

Influence of crystallite size and temperature on the antiferromagnetic helices of terbium and holmium metal

A. Michels* and J.-P. Bick

Technische Physik, Universität des Saarlandes, Postfach 151150, D-66041 Saarbrücken, Germany and Laboratory for the Physics of Advanced Materials, University of Luxembourg, 162A Avenue de la Faïencerie, L-1511 Luxembourg, Luxembourg

R. Birringer and A. Ferdinand

Technische Physik, Universität des Saarlandes, Postfach 151150, D-66041 Saarbrücken, Germany

J. Baller and R. Sanctuary

Laboratory for the Physics of Advanced Materials, University of Luxembourg, 162A Avenue de la Faïencerie, L-1511 Luxembourg, Luxembourg

S. Philippi

Leibniz Institute for Solid State and Materials Research, Helmholtzstraße 20, D-01069 Dresden, Germany

D. Lott

GKSS Research Center, Max-Planck-Straße 1, D-21502 Geesthacht, Germany

S. Balog

Paul Scherrer Institut, CH-5232 Villigen PSI, Switzerland

E. Rotenberg

Advanced Light Source, Lawrence Berkeley National Laboratory, Berkeley, California 94720, USA

G. Kaindl

Institut für Experimentalphysik, Freie Universität Berlin, Arnimallee 14, D-14195 Berlin-Dahlem, Germany

K. M. Döbrich

Max-Born-Institut, Max-Born-Straße 2A, D-12489 Berlin, Germany and Institut für Experimentalphysik, Freie Universität Berlin, Arnimallee 14, D-14195 Berlin-Dahlem, Germany

(Received 14 December 2010; revised manuscript received 18 April 2011; published 23 June 2011)

We report on the results of grain-size and temperature-dependent magnetization, specific-heat, and neutron-scattering experiments on the heavy rare-earth metals terbium and holmium, with particular emphasis on the temperature regions where the helical antiferromagnetic phases exist. In contrast to Ho, we find that the helical structure in Tb is relative strongly affected by microstructural disorder, specifically, it can no longer be detected for the smallest studied grain size of $D = 18$ nm. Moreover, in coarse-grained Tb a helical structure persists even in the ferromagnetic regime, down to about $T = 215$ K, in agreement with angle-resolved photoelectron spectroscopy (ARPES) data, which reveal a nesting feature of the bulk Fermi surface at the L point of the Brillouin zone at $T = 210$ K. As samples for the ARPES measurements, we used 10-nm-thick single-crystalline Tb films that show a bulk electronic valance-band structure. Thus our ARPES measurements are used to discuss temperature-induced effects observed in the coarse-grained samples.

DOI: [10.1103/PhysRevB.83.224415](https://doi.org/10.1103/PhysRevB.83.224415)

PACS number(s): 61.05.fg, 71.18.+y, 71.20.Eh, 75.25.-j

I. INTRODUCTION

Magnetism of the heavy Lanthanide (Ln) metals is still a fascinating field of basic condensed-matter research despite the fact that most of these elements have already been discovered in the 19th century and that a great deal of mature knowledge regarding their magnetic ground states has been accumulated during the second half of the past century.¹⁻⁴ Present research and open problems address, e.g., the temperature dependence of the exchange splitting of Gd⁵ and Tb⁶ surface states, the critical behavior,⁷⁻⁹ the origin of magnetic anisotropy¹⁰ and the electronic band structure¹¹⁻¹³ of Gd, the influence of film

thickness on the critical behavior of Gd and Ho films,¹⁴⁻¹⁶ the issue of field-induced chirality in the helix structure of Dy/Y multilayers,¹⁷ or the field-dependent magnetic ordering in Eu films.¹⁸

The magnetism of the Ln metals originates from the electrons in the partially filled $4f$ shell, which give rise to localized magnetic moments that couple via the long-range Ruderman-Kittel-Kasuya-Yosida (RKKY) interaction involving conduction electrons.¹⁻⁴ The knowledge of the topology of the Fermi surface (FS) is crucial for an understanding of the low-energy excitation properties of metallic materials. This is particularly so for the heavy Ln metals,

where the electrons at the Fermi energy E_F play a decisive role in establishing long-range magnetic order (see, e.g., Refs. 19–25, and references therein). Indeed, only minor differences in the shape of the FS result in a variety of complex spin structures, including paramagnetic (PM), ferromagnetic (FM), helical antiferromagnetic (AFM), ferrimagnetic conical, oscillatory spin-wave-like, and antiphase-domain-like phases.²⁶

The PM-AFM phase transition at the Néel temperature T_N for some of the heavy Ln metals is widely believed to be driven by FS nesting—i.e., parallel sheets of the respective FS in the PM phase that are connected with the reciprocal vector \mathbf{q}_0 —which has recently been observed for Tb.²⁵ The connection between FS nesting and helical AFM, where \mathbf{q}_0 corresponds to the wave vector of the AFM helix \mathbf{q}_H ,²² is commonly referred to as the *nesting hypothesis*.

From an experimental point of view, manipulation of the topology of the FS is feasible through the application of external forces or fields (e.g., Refs. 19,21,27–29). In this paper, we adopt a different approach and investigate the influence of *nanocrystallinity* on the stability of the helix structures in Tb and Ho. The downscaling of the average crystallite size D in a polycrystalline bulk material to the nm scale has mainly two consequences for the magnetic properties: (i) the reduction of D results in an increase of the interface-to-volume ratio and in concomitant interface-induced spin disorder;³⁰ (ii) crossing length scales may appear in the system, i.e., the “correlation” length of the microstructure—the grain size D —may become comparable to or even smaller than an intrinsic magnetic length scale, here, the wavelength λ_H of the helical AFM spin structure. For Tb single crystals, λ_H is weakly dependent on temperature and takes on values of $\lambda_H \cong 50\text{--}55$ Å for $T_c \lesssim T \lesssim T_N$,³¹ whereas for Ho single crystals, λ_H changes from $\cong 20$ Å at $T_N \cong 133$ K to $\cong 35$ Å at 4.2 K.³²

II. EXPERIMENT

Nanocrystalline Tb and Ho samples, with as-prepared average crystallite sizes D in the 10–20-nm range, were synthesized by means of the inert-gas condensation technique,³³ the purity of both starting materials (as specified by the supplier) was 99.9 at. % with respect to metallic impurities. The distribution of grain sizes resulting from this synthesis route was found to be of the log-normal type.^{33,34} Coarsening of the grain microstructure (grain growth)^{35,36} was achieved by heat treatments under vacuum ($p < 10^{-5}$ mbar) at typical annealing temperatures of 100–400 °C (annealing time: 1 h). The mass density of the samples was measured by the Archimedes method and found to be 98–99% of the bulk value, indicating low porosity. Average crystallite sizes and microstrain were determined by wide-angle x-ray diffraction according to the Williamson-Hall method.³⁷ The values for the root-mean-square (rms) microstrain of as-prepared Tb and Ho samples are of the order of several 0.1%. rms microstrain is generic of any polycrystalline material but becomes particularly pronounced in nanocrystalline metals; it scales as $1/D$ and thus becomes negligibly small for $D \gtrsim 100$ nm.³⁸ In the following, the notation “ $D > 100$ nm” refers to coarse-grained samples with diffractograms that can

no longer be distinguished from the resolution function of the diffractometer. For further details on sample preparation and microstructural characterization, we refer to Refs. 39 and 40. ac and dc magnetization data were recorded with a PPMS model 6000 extraction magnetometer. Measurements of the specific-heat capacity were performed by temperature modulated differential scanning calorimetry (TM-DSC) using a DSC821e setup (from Mettler Toledo, Switzerland).

The neutron-scattering experiments were carried out at the NeRo reflectometer at the Geesthacht Neutron Facility (GeNF), Geesthacht, Germany, and at the Swiss spallation neutron source (SINQ, Paul Scherrer Institut, Switzerland), using the SANS-II beamline.⁴¹ At GeNF, we used incident neutrons with a mean wavelength of $\lambda = 4.335$ Å ($\Delta\lambda/\lambda \leq 2\%$), whereas at PSI, $\lambda = 4.7$ Å ($\Delta\lambda/\lambda = 10\%$) and $\lambda = 9.1$ Å ($\Delta\lambda/\lambda = 10\%$). In both neutron experiments, the scattering along the forward direction was measured. The uncertainty in the temperature value is about ± 1 K.

The angle-resolved photoelectron spectroscopy (ARPES) measurements were performed at beamline 7.0.1 of the Advanced Light Source, Lawrence Berkeley National Laboratory, USA. In contrast to the magnetization and neutron experiments, where polycrystalline bulk samples were studied, we used single-crystalline 10-nm-thick Tb metal films in the ARPES measurements, prepared *in situ* on a W(110) single crystal. It has been shown in previous ARPES experiments²³ that films of this thickness show a bulk electronic valence-band structure. Note that at film thicknesses > 5 nm, the electronic structure as seen with ARPES does not depend on the film thickness; because of the surface sensitivity of this technique only the first few top layers contribute to the measured signal. Our ARPES results thus have to be compared to the results of coarse-grained samples in our complementary experiments on polycrystalline Tb. The single crystallinity of the samples was checked with low-energy electron diffraction. In our photoelectron spectra (base pressure in analysis chamber: 10^{-11} mbar), we observed well-ordered, clean surfaces, as can be seen, e.g., from the surface-core-level shift of the $^8S_{7/2}$ component of the $4f$ states of 0.26 ± 0.01 eV (not shown), in very good agreement with Ref. 42. We used linearly polarized photons in the energy range from 85 to 135 eV to measure a series of photoelectron spectra (energy distribution curves) with a total-system energy resolution of about 50 meV (full width at half maximum). The samples were mounted on a low-temperature goniometer, providing all three angular degrees of freedom. We rotated the sample with 0.25° steps at various photon energies to get access to the electronic structure covering a full Brillouin zone (BZ). The data were subsequently transformed to \mathbf{k} space using simple spherical transformations. Here, we show data representing the photoemission intensity at $E = E_F$ at various data points, revealing the shape of the FS within a full BZ. Further details on experimental procedures and data analysis are given elsewhere.^{23–25}

III. RESULTS AND DISCUSSION

Figure 1 displays the temperature- and grain-size-dependent ac susceptibility χ of Ho and Tb metal. The susceptibility of Ho is only rather weakly influenced by

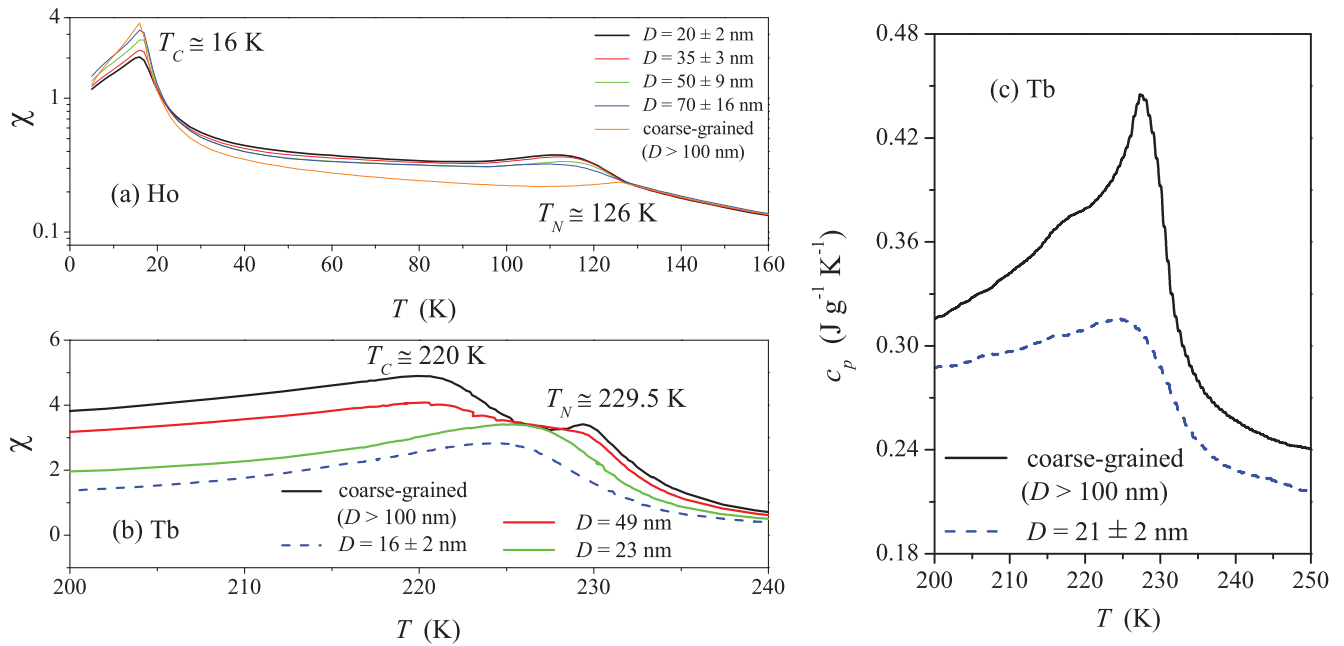


FIG. 1. (Color online) Temperature and grain-size dependence of the ac susceptibility χ of (a) Ho (log-linear scale) and (b) Tb (ac field amplitude: 10 Oe; ac field frequency: 100 Hz). The approximate peak positions in the $\chi(T)$ curves for the coarse-grained samples are given in (a) and (b). (c) Temperature and grain-size dependence of the specific-heat capacity $c_p(T)$ of Tb metal (TMDSC modulation period: 120 s; temperature amplitude: 0.5 K; heating rate: 0.5 K/min).

the small grain size [Fig. 1(a)]. Here, the reduction of D to the nm scale mainly has an impact on the position of T_N , whereas T_c remains almost constant. Furthermore, for $T_c \lesssim T \lesssim T_N$, $\chi(T)$ of Ho increases with decreasing D . This observation is explained by an increasingly large fraction of uncompensated magnetic moments arising from interface regions, which develops with decreasing grain size.

By contrast, the susceptibility of Tb is strongly affected by the downscaling of D to the nm range [Fig. 1(b)]: while coarse-grained Tb exhibits two peaks in χ at the characteristic transition temperatures of the single crystal, $T_N \cong 229.5$ K and $T_c \cong 220$ K,³ Tb with $D = 16$ nm reveals only a single peak in χ at about 224 K. Furthermore, $\chi(T)$ of Tb is

consistent with the temperature variation of the specific-heat capacity $c_p(T)$ [Fig. 1(c)], which for the coarse-grained material exhibits a pronounced λ anomaly at about 228 K. Note that the first-order transition at T_c is only weakly resolved in the $c_p(T)$ data of coarse-grained Tb, in agreement with literature data for polycrystalline Tb.^{43,44}

For coarse-grained (well-annealed) Ho and Tb, we find the transition temperatures [Figs. 1(a) and 1(b)] as well as the value of the effective magnetic moment in the paramagnetic regime (Fig. 2 in Ref. 29) of high-purity bulk single crystals. These results suggest that impurities have a negligible influence on the bulk magnetic properties of the inert-gas condensed samples of the present study.^{30,39,40}

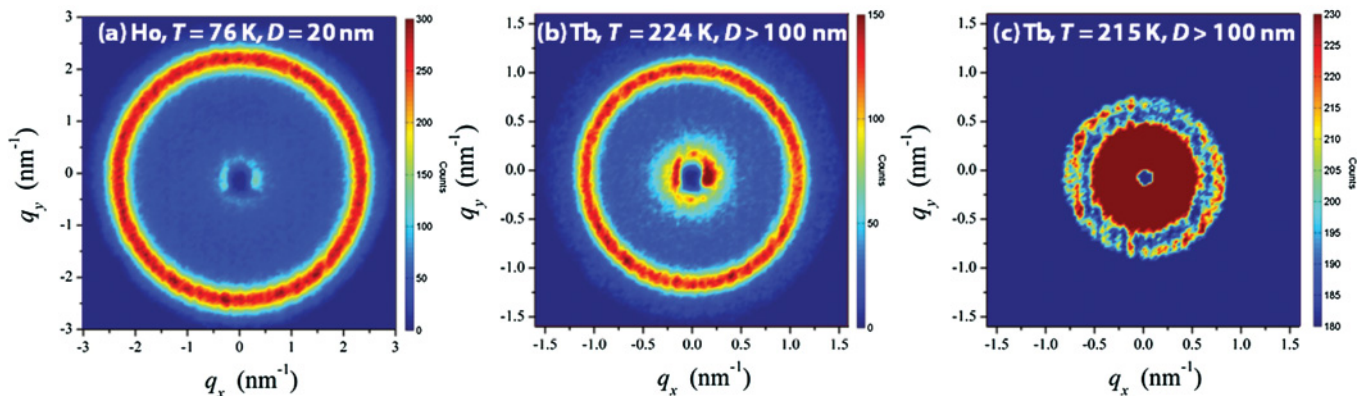


FIG. 2. (Color online) Color-coded maps of the neutron-intensity distribution on a two-dimensional (2D) position-sensitive detector: (a) Ho with $D = 20$ nm at $T = 76$ K; (b) Tb with $D > 100$ nm at $T = 224$ K; (c) Tb with $D > 100$ nm at $T = 215$ K. The outermost rings in (a)–(c) can be assigned to magnetic scattering due to helical AFM structures. Within the small-angle approximation, the scattering vector is given by $\mathbf{q} \cong (q_x, q_y, 0)$, where the wave vector of the incident neutron beam is taken along the z direction.

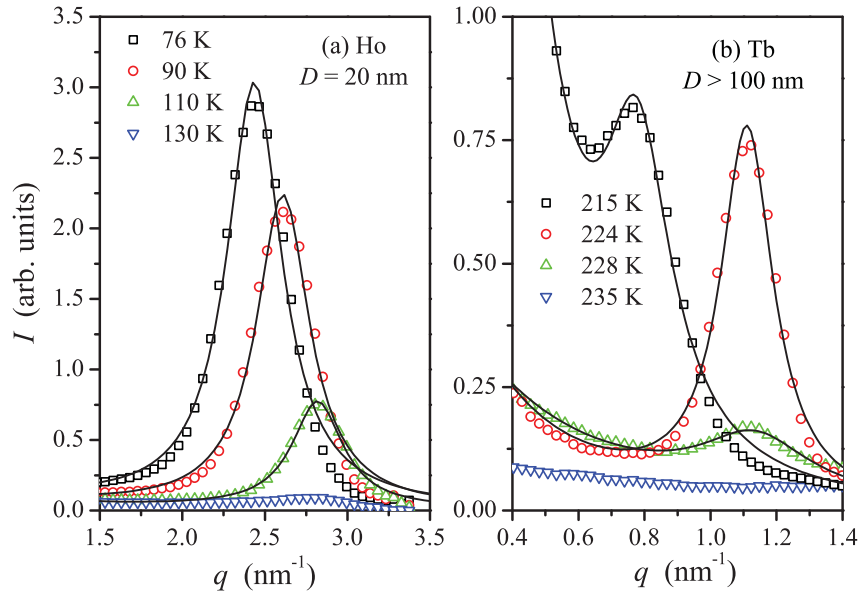


FIG. 3. (Color online) Azimuthally averaged neutron-scattering intensity as a function of momentum transfer $q = \frac{4\pi}{\lambda} \sin \theta$ and temperature (see inset): (a) Ho with $D = 20 \pm 2$ nm; (b) Tb with $D > 100$ nm (2θ : scattering angle). The solid lines in (a) and (b) represent fit results of Eq. (1) to the data.

The observation of a single peak in $\chi(T)$ of Tb at $T = 224$ K for $D = 16$ nm was interpreted in Ref. 29 by the absence of a helical AFM phase. Possible origins were attributed to internal magnetostatic fields due to interface-induced spin disorder⁴⁵ and to the crossing-length scales scenario. Note that the ratio of the smallest experimental grain size and the wavelength of the helix, D/λ_H , is about 3–4 in the case of Tb and $D/\lambda_H \cong 8$ –10 for Ho.

A direct method for studying the grain-size dependence of the helical AFM structure is given by Bragg diffraction, since the magnetic scattering cross section $d\sigma_M/d\Omega \propto \delta[\mathbf{q} - (\mathbf{G} \pm \mathbf{q}_H)]$, where \mathbf{q} denotes the scattering vector, \mathbf{G} is a reciprocal-lattice vector, and \mathbf{q}_H is the wave vector of the helix.⁴⁶ Figures 2 and 3 display typical small-angle neutron-scattering data [around $\mathbf{G} = (0,0,0)$],^{47–49} and Fig. 4 gives the results for the variation of the interlayer turn angle φ in Ho and Tb as a function of T and D . The turn angle was calculated according to $\varphi = \frac{1}{2} c q_m$, where c is the hcp lattice constant and q_m denotes the position of the Bragg peak due to coherent magnetic scattering of neutrons on the helix; q_m was determined by fitting the azimuthally averaged neutron data to the following phenomenological expression for $I(q) \propto d\sigma_M/d\Omega$ (compare solid lines in Fig. 3):

$$I(q) = \frac{a}{q^n} + \frac{I_0 \sigma^2}{\sigma^2 + (q - q_m)^2}. \quad (1)$$

The quantities a, n, I_0, σ , and q_m in Eq. (1) are adjustable parameters.

Magnetic Bragg peaks were observed for all Ho samples with $D \gtrsim 20$ nm and for temperatures between 70 K $\lesssim T \lesssim T_N$. The effect of grain size on the turn angle φ in Ho is relatively weak within the studied temperature range [Fig. 4(a)], and our results for $\varphi(T, D)$ essentially reproduce the single-crystal data.³²

In accordance with the magnetic susceptibility data, we did not find a helical structure in Tb for the smallest grain size of

$D = 18$ nm. An indication for the existence of a residual spin helix was found for a Tb specimen with an average grain size of 30 nm (data not shown here); the relatively poor statistics of the data did not allow a reliable determination of φ . In contrast to Ho, the turn angle in Tb (and its temperature variation) appears to be significantly different from the literature data for bulk single crystals³¹ [Fig. 4(b)]. However, one should take into account that the reported value of the Néel point of the Tb single crystal used in the neutron study of Ref. 31 was $T_N = 226$ K, i.e., 4 K below the accepted literature value, a fact that hints on the presence of a significant amount of impurities in the studied sample.⁵⁰ Different from the literature data, we do not observe an increase of φ in Tb at the smallest T ,

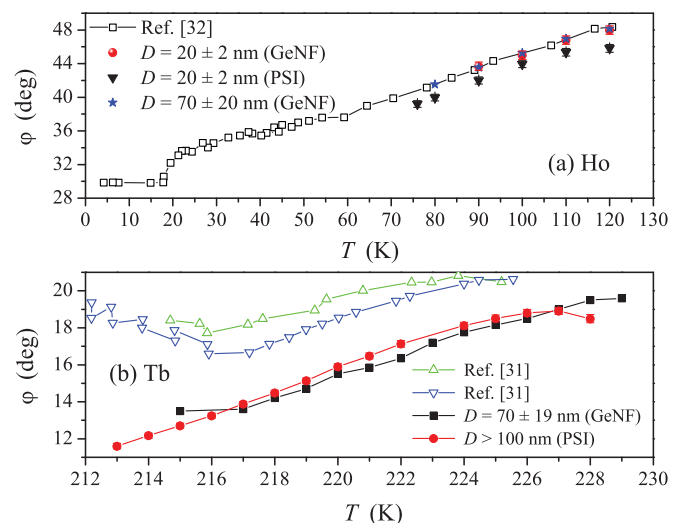


FIG. 4. (Color online) Temperature and grain-size dependence of the helix turn angle φ : (a) Ho; (b) Tb; in both cases with comparisons to literature data. Lines are guides to the eyes. We also compare data for φ obtained on different neutron instruments (at GeNF and PSI).

but a smooth decrease for temperatures below $T_c \cong 220$ K. A magnetic Debye-Scherrer ring is clearly observed for coarse-grained Tb at $T = 215$ K [Figs. 2(c) and 3(b)]. This suggests that the phase transition to the ferromagnetically ordered state is smeared out over a relatively large temperature range.

Our observation of a residual spin helix in coarse-grained Tb metal below T_c at 215 K is in line with measurements of the bulk FS topology that is obtained with ARPES. For the development of an AFM helix—according to the nesting hypothesis—the shape of the FS has to include sections that allow for nesting. The Tb FS slightly below T_c at 210 K (Fig. 5) shows such sections close to the L point of the hexagonal Brillouin zone. The nesting vector $\mathbf{q}_0 = 0.2 \pm 0.1 \text{ \AA}^{-1}$ is comparable with the one found for the PM phase²⁵ within experimental error bars (induced by the momentum broadening in ARPES perpendicular to the surface²³), corresponding to $\varphi = 30 \pm 15^\circ$, in reasonable agreement with our neutron-scattering data. At $T = 210$ K, the topology of the FS resembles that in the PM phase [see Fig. 1(b) in Ref. 25], broadened by the increased magnetic exchange splitting $\Delta E_{ex} \cong 0.3 \text{ eV}$,⁵¹ indicating the onset of the separation of majority and minority FS sheets. Further cooling down of the sample increases ΔE_{ex} that—at slightly lower temperatures—fully lifts the spin degeneracy of the FS sheets and then forces nesting to disappear completely [Figs. 3 and 4 in Ref. 25]. This mechanism acts as a major driving force behind the AFM-to-FM phase transition.

The results presented in Fig. 5 in conjunction with the data in Ref. 25, however, show that the transitions of the shape of the FS do not occur abruptly at T_N and T_c , respectively. The transition of the FS topology occurs in a rather soft manner, with a slowly increasing ΔE_{ex} with decreasing temperature that gradually modifies the shape of the FS. In this way, the FS-nesting-induced driving force toward an AFM helix gets slowly weaker, to the point at T_c , where other energetic

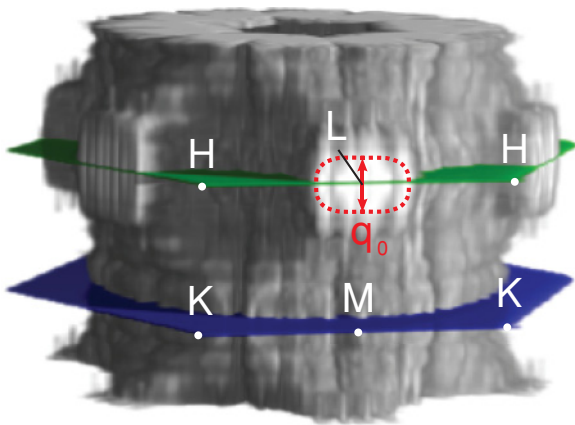


FIG. 5. (Color online) Regions of high PE intensity at $E = E_F$ for Tb metal, reflecting the FS at $T = 210 \pm 5$ K in the ferromagnetic phase, slightly below T_c . FS sheets that allow for nesting are observed around the L point of the Brillouin zone, i.e., horizontal sections of the dotted line that marks the region of highest photoemission intensities and serves as a guide to the eyes. Note that high (low) PE intensity corresponds to light-gray (dark-gray) tones.

contributions in favor of a FM ordering become stronger (e.g., the magnetocrystalline anisotropy that favors certain orientations of the magnetization along discrete easy axes). Despite an overall FM ordering at temperatures slightly below T_c , there is a residual FS nesting and therefore a residual spin helix in Tb metal, both observed by means of ARPES and neutron scattering, respectively.

IV. SUMMARY AND CONCLUSIONS

In summary, we have studied the grain-size and temperature dependence of the helical antiferromagnetic (AFM) phases of the heavy lanthanide metals terbium and holmium by employing a wide range of complementary techniques such as ac susceptibility, specific heat, and neutron scattering. To investigate the origin of the helical ordering, we also performed measurements of the bulk electronic structure of Tb by means of angle-resolved photoelectron spectroscopy. We have found strong evidence that the AFM helix in nanocrystalline Tb (with a distribution of crystallite sizes) is suppressed if the average grain size D is of the order of the helix wavelength λ_H , specifically for a ratio $D/\lambda_H = 3-4$. At similar crystallite sizes, the helix in Ho does not disappear for the smallest studied grain sizes of $D/\lambda_H = 8-10$ (due to a smaller λ_H). Furthermore, we show that for Tb with larger crystallite sizes, a residual AFM helix and, correspondingly, a nesting-type Fermi surface can be found even at temperatures slightly below T_c , despite an overall FM ordering. The turn angle per monolayer φ decreases continuously with temperature from T_N to below T_c , in contrast to previously reported bulk data, where an increase in φ had been observed for temperatures below T_c . Our results provide further evidence for the view that the magnetic phase transitions in heavy Ln metals are governed by a delicate interplay between various energy contributions. Changes of the ordering parameters, e.g., φ , as well as a transition of the shape of the Fermi surface do not occur sharply, at T_N and T_c , respectively. The PM-AFM and the AFM-FM phase transitions are rather stretched over a broad temperature region and occur in a relatively soft manner.

ACKNOWLEDGMENTS

We thank F. Döbrich for critically reading the manuscript and we acknowledge contributions by K. Starke (deceased) in the early stages of this work. This study was financially supported by the European Commission (Contract No. RII-CT-2003-505925), by the Deutsche Forschungsgemeinschaft (Grants No. MI 738/3-2, No. MI 738/6-1, and No. STA 413/3-1), the U.S. Department of Energy under Contract No. DEAC03-76SF00098, and by the National Research Fund of Luxembourg in the framework of ATTRACT Project No. FNR/A09/01. Part of the work is based on experiments performed at the Swiss spallation neutron source SINQ, Paul Scherrer Institute, Villigen, Switzerland.

*andreas.michels@uni.lu

- ¹R. J. Elliot, in *Magnetism*, Vol. II, part A, edited by G. T. Rado and H. Suhl (Academic Press, New York, 1965), pp. 385–425.
- ²A. J. Freeman, in *Magnetic Properties of Rare Earth Metals*, edited by R. J. Elliot (Plenum Press, London, 1972).
- ³S. Legvold, in *Ferromagnetic Materials*, edited by E. P. Wohlfarth, Vol. 1 (North-Holland, Amsterdam, 1980), pp. 183–295.
- ⁴J. Jensen and A. R. Mackintosh, *Rare Earth Magnetism* (Clarendon, Oxford, 1991).
- ⁵M. Donath, B. Gubanka, and F. Passek, *Phys. Rev. Lett.* **77**, 5138 (1996).
- ⁶M. Bode, M. Getzlaff, A. Kubetzka, R. Pascal, O. Pietzsch, and R. Wiesendanger, *Phys. Rev. Lett.* **83**, 3017 (1999).
- ⁷E. Frey, F. Schwabl, S. Henneberger, O. Hartmann, R. Wäppling, A. Kratzer, and G. M. Kalvius, *Phys. Rev. Lett.* **79**, 5142 (1997).
- ⁸J. M. D. Coey, V. Skumryev, and K. Gallagher, *Nature (London)* **401**, 35 (1999).
- ⁹S. N. Kaul and S. Srinath, *Phys. Rev. B* **62**, 1114 (2000).
- ¹⁰M. Colarieti-Tosti, S. I. Simak, R. Ahuja, L. Nordström, O. Eriksson, D. Åberg, S. Edvardsson, and M. S. S. Brooks, *Phys. Rev. Lett.* **91**, 157201 (2003).
- ¹¹P. Kurz, G. Bihlmayer, and S. Blügel, *J. Phys.: Condens. Matter* **14**, 6353 (2002).
- ¹²I. Turek, J. Kudrnovský, G. Bihlmayer, and S. Blügel, *J. Phys.: Condens. Matter* **15**, 2771 (2003).
- ¹³C. Santos, W. Nolting, and V. Eyert, *Phys. Rev. B* **69**, 214412 (2004).
- ¹⁴M. Farle, K. Baberschke, U. Stetter, A. Aspelmeier, and F. Gerhardter, *Phys. Rev. B* **47**, 11571 (1993).
- ¹⁵M. Gajdzik, T. Trappmann, C. Sürgers, and H. v. Löhneysen, *Phys. Rev. B* **57**, 3525 (1998).
- ¹⁶E. Weschke, H. Ott, E. Schierle, C. Schüßler-Langeheine, D. V. Vyalikh, G. Kaindl, V. Leiner, M. Ay, T. Schmitte, H. Zabel, and P. J. Jensen, *Phys. Rev. Lett.* **93**, 157204 (2004).
- ¹⁷S. V. Grigoriev, Y. O. Chetverikov, D. Lott, and A. Schreyer, *Phys. Rev. Lett.* **100**, 197203 (2008).
- ¹⁸S. Soriano, C. Dufour, K. Dumesnil, and P. Mangin, *Eur. Phys. J. B* **63**, 469 (2008).
- ¹⁹A. V. Andrianov, D. I. Kosarev, and A. I. Beskrovnyi, *Phys. Rev. B* **62**, 13844 (2000).
- ²⁰S. J. Crowe, S. B. Dugdale, Z. Major, M. A. Alam, J. A. Duffy, and S. B. Palmer, *Europhys. Lett.* **65**, 235 (2004).
- ²¹F. Heigl, J. E. Prieto, O. Krupin, K. Starke, G. Kaindl, and M. Bode, *Phys. Rev. B* **72**, 035417 (2005).
- ²²I. D. Hughes, M. Däne, A. Ernst, W. Hergert, M. Lüders, J. Poulter, J. B. Staunton, A. Svane, Z. Szotek, and W. M. Temmerman, *Nature (London)* **446**, 650 (2007).
- ²³K. M. Döbrich, G. Bihlmayer, K. Starke, J. E. Prieto, K. Rossnagel, H. Koh, E. Rotenberg, S. Blügel, and G. Kaindl, *Phys. Rev. B* **76**, 035123 (2007).
- ²⁴K. M. Döbrich, A. Bostwick, E. Rotenberg, and G. Kaindl, *Phys. Rev. B* **81**, 012401 (2010).
- ²⁵K. M. Döbrich, A. Bostwick, J. L. McChesney, K. Rossnagel, E. Rotenberg, and G. Kaindl, *Phys. Rev. Lett.* **104**, 246401 (2010).
- ²⁶W. C. Koehler, *J. Appl. Phys.* **36**, 1078 (1965).
- ²⁷N. Achiwa, S. Kawano, A. Onodera, and Y. Nakai, *J. Phys. Colloq.* **49**, C8-349 (1988).
- ²⁸D. D. Jackson, V. Malba, S. T. Weir, P. A. Baker, and Y. K. Vohra, *Phys. Rev. B* **71**, 184416 (2005).
- ²⁹S. Philippi, J. Markmann, R. Birringer, and A. Michels, *J. Appl. Phys.* **105**, 07A701 (2009).
- ³⁰F. Döbrich, M. Elmas, A. Ferdinand, J. Markmann, M. Sharp, H. Eckerlebe, J. Kohlbrecher, R. Birringer, and A. Michels, *J. Phys.: Condens. Matter* **21**, 156003 (2009).
- ³¹O. W. Dietrich and J. Als-Nielsen, *Phys. Rev.* **162**, 315 (1967).
- ³²W. C. Koehler, J. W. Cable, M. K. Wilkinson, and E. O. Wollan, *Phys. Rev.* **151**, 414 (1966).
- ³³R. Birringer, *Mater. Sci. Eng.* **117**, 33 (1989).
- ³⁴C. E. Krill and R. Birringer, *Philos. Mag. A* **77**, 621 (1998).
- ³⁵A. Michels, C. E. Krill, H. Ehrhardt, R. Birringer, and D. T. Wu, *Acta Mater.* **47**, 2143 (1999).
- ³⁶C. E. Krill III, L. Helfen, D. Michels, H. Natter, A. Fitch, O. Masson, and R. Birringer, *Phys. Rev. Lett.* **86**, 842 (2001).
- ³⁷H. P. Klug and L. E. Alexander, *X-Ray Diffraction Procedures for Polycrystalline and Amorphous Materials* (Wiley, New York, 1974), Chap. 9.
- ³⁸M. Ames, J. Markmann, R. Karos, A. Michels, A. Tschöpe, and R. Birringer, *Acta Mater.* **56**, 4255 (2008).
- ³⁹D. Michels, C. E. Krill III, and R. Birringer, *J. Magn. Magn. Mater.* **250**, 203 (2002).
- ⁴⁰J. Weissmüller, A. Michels, D. Michels, A. Wiedenmann, C. E. Krill III, H. M. Sauer, and R. Birringer, *Phys. Rev. B* **69**, 054402 (2004).
- ⁴¹P. Strunz, K. Mortensen, and S. Janssen, *Physica B* **350**, e783 (2004).
- ⁴²E. Navas, K. Starke, C. Laubschat, E. Weschke, and G. Kaindl, *Phys. Rev. B* **48**, 14753 (1993).
- ⁴³L. D. Jennings, R. M. Stanton, and F. H. Spedding, *J. Chem. Phys.* **27**, 909 (1957).
- ⁴⁴T. J. McKenna, S. J. Campbell, D. H. Chaplin, and G. V. H. Wilson, *Solid State Commun.* **40**, 177 (1981).
- ⁴⁵A. Michels, J. Weissmüller, and R. Birringer, *Eur. Phys. J. B* **29**, 533 (2002).
- ⁴⁶G. L. Squires, *Introduction to the Theory of Thermal Neutron Scattering* (Dover, New York, 1978).
- ⁴⁷A. Michels, J. Weissmüller, A. Wiedenmann, and J. G. Barker, *J. Appl. Phys.* **87**, 5953 (2000).
- ⁴⁸A. Michels, R. N. Viswanath, and J. Weissmüller, *Europhys. Lett.* **64**, 43 (2003).
- ⁴⁹A. Michels and J. Weissmüller, *Rep. Prog. Phys.* **71**, 066501 (2008).
- ⁵⁰D. C. Jiles, S. B. Palmer, D. W. Jones, S. P. Farrant, and K. A. Gschneidner Jr., *J. Phys. F* **14**, 3061 (1984).
- ⁵¹C. Schüßler-Langeheine, E. Weschke, C. Mazumdar, R. Meier, A. Y. Grigoriev, G. Kaindl, C. Sutter, D. Abernathy, G. Grübel, and M. Richter, *Phys. Rev. Lett.* **84**, 5624 (2000).